Discrete dislocation, crystal plasticity and experimental studies of fatigue crack nucleation in single-crystal nickel

Nikoletta G. Prastiti[1], Yilun Xu[2], Daniel S. Balint[1], and Fionn P.E. Dunne[2]
[1]Department of Mechanical Engineering, Imperial College, London SW7 2AZ, UK
[2]Department of Materials, Imperial College, London SW7 2AZ, UK

Abstract

Dislocation configurational energy and stored energy densities are determined in discrete dislocation and crystal plasticity modelling respectively and assessed with respect to experiments on single crystal nickel fatigue crack nucleation. Direct comparisons between the three techniques are provided for two crystal orientation fatigue tests. These provide confirmation that both quantities correctly identify the sites of fatigue crack nucleation and that stored energy density is a reasonable approximation to the more rigorous dislocation configurational energy. GND density is shown to be important in locating crack nucleation sites because of its role in the local configurational energy density.

Keywords:
Fatigue crack nucleation; Crystal plasticity; Dislocations; Stored energy; Configurational energy; Nickel superalloys

Highlights:

- Integrated experimental and computational study of fatigue crack nucleation in two nickel single crystals using discrete dislocation plasticity and crystal plasticity.
- Successful identification of the crack nucleation sites in both single crystals using the configurational energy density from discrete dislocation plasticity and the stored energy density from crystal plasticity.
- GND density plays a significant role in the identification of crack nucleation sites at the micron length scale.
- Microstructural quantities such as lattice rotation, principle stress, effective strain and SSD density cannot in their own right predict the crack initiation sites.

1 Introduction

Considerable progress has been made over the years in predicting fatigue crack propagation (Carpinteri, 1994; Krupp, 2007; Paris and Erdogan, 1963; Tomkins, 1968), but the accurate prediction of fatigue crack nucleation remains elusive to this day. One of the main reasons hindering the development of a unified fatigue crack nucleation theory lies in the complexity of microstructure and the lack of mechanistic understanding behind the behaviour of materials across length and time scales. This paper aims to bridge the gap between experimental observations of fatigue crack nucleation in single crystal nickel-based superalloys and mechanistic insights drawn from energy formulations defined within a crystal plasticity and a discrete dislocation plasticity framework.

In recent work (Zheng et al., 2019), a new quantity termed configurational energy density of dislocations was proposed and introduced ideas for the mechanistic drivers of microstructurally-sensitive fatigue crack nucleation and growth (Wilson et al., 2018). The area over which the configurational energy of dislocations is stored was argued to have mechanistic significance. The progressive increase in configurational energy with cyclic loading at specific locations within the microstructure suggests a potential relationship between the energy balance associated with the new free surface energy and the release of dislocation configurational energy rate per unit crack area. The role of geometrically necessary dislocation (GND) density was associated with some of the dislocation structures giving rise to high local energy density. The discrete dislocation configurational energy density was also shown to be reasonably captured by stored energy density within crystal plasticity modelling, thereby providing a higher length scale modelling method to address fatigue crack nucleation and growth. The stored energy density criterion proposed by (Wan et al., 2014) unifies contributions from local slip accumulation, stress and dislocation density and has been employed in several studies to successfully identify the experimentally observed sites of fatigue crack nucleation in steel (Wan et al., 2016b, 2014) and nickel (Chen et al., 2018, 2017).

The observation that dislocations play a central role in fatigue damage development in metals led many researchers to derive analytical theories and criteria associated with dislocation arrangements and their role in fatigue crack nucleation. For example, (Tanaka and Mura, 1981) modelled the extrusions and intrusions forming on the surface of fatigued metals using dislocation pileups and then used an energy balance to predict crack initiation in favourably

oriented grains. However, it has been reported that such formulations are very rarely applied to structural alloys (Chan, 2010). Surface roughness as an outcome of dislocations exiting through the free surface of metals has also been used as a criterion for fatigue crack nucleation. (Harvey et al., 1994) used atomic force microscope in titanium and HSLA steel to derive a crack initiation criterion based on the formation of slip steps during strain cycling. Crack initiation was assumed to occur once the cumulative slip-height displacement exceeded a threshold value. The advent of powerful microscopy has enabled the detection of dislocation patterning during cyclic loading which could be used as a tool to predict fatigue crack nucleation (Grilli et al., 2018; Hussein and El-Awady, 2016; Irastorza-Landa et al., 2016; Laird and Feltner, 1968; Mughrabi, 1983; Polák et al., 1993). In addition, it potentially provides mechanistic insight in to the drivers of the crack nucleation process.

Numerical investigations of dislocation structures at the micron length-scale and their influence in fatigue crack nucleation have been limited. (Amodeo and Ghoniem, 1990) used dislocation dynamics to explicitly model persistent slip bands and showed that their formation is an outcome of the competition between dipole formation and annihilation of dislocations of opposite Burgers vectors at low temperatures. (Deshpande et al., 2004) used a cohesive surface constitutive relation so that crack initiation and growth emerge as natural outcomes of discrete dislocation simulations. (Brinckmann and Giessen, 2007) used discrete dislocation plasticity incorporating cohesive zones and surface roughening to study fatigue crack initiation. (Déprés et al., 2004) used 3-D discrete dislocation simulations to model damage accumulation mechanisms in high cycle fatigue and managed to reproduce dislocation structures observed in the experiments. In addition, they argued that the plastic shear accumulating within the slip bands may be used as a crack initiation criterion. However, it is not clear when these dislocation structures begin to form a crack surface (Heinrich and Sundararaghavan, 2017). The latter authors used 3-D dislocation simulations to predict fatigue crack initiation in which their crack nucleation criterion requires the insertion of a hypothetical crack in the material and the calculation of a Gibbs energy balance to form a new surface. Undoubtedly discrete dislocation modelling has contributed in the mechanistic understanding of fatigue crack nucleation (McDowell and Dunne, 2010; Sangid, 2013; Suresh, 1998) and the sequence of events leading to crack initiation in metals is much better understood as a result of dislocation simulations (Déprés et al., 2014). However, the direct

assessment of dislocation-based modelling of fatigue crack nucleation, and configurational energy in particular, with respect to single crystal experiments has not so far been addressed. The work presented in this paper, is both an extension and advance of our previous work in (Zheng et al., 2019). More specifically, it provides a direct comparison between discrete dislocation plasticity, crystal plasticity and experimental evidence on fatigue damage development in two nickel single crystals, corroborating the argument that the configurational energy is indeed a fundamental driver of fatigue crack nucleation at the micron length scale. Furthermore, it assesses other microstructural quantities including dislocation density (both SSD and GND), average lattice rotation, average strain, and average stress, in the context of accurately predicting the location of crack nucleation sites.

The paper is structured as follows. The next sections introduce the CPFE and DD methodologies, and an overview of previous experimental observations. The CPFE and DD geometric model constructions are then presented, followed by both qualitative and quantitative assessment of predicted and experimentally observed slip fields and fatigue crack nucleation sites.

2 Methodology

2.1 Crystal plasticity finite element modelling

A dislocation-based crystal plasticity finite element framework is utilised and briefly summarised but full detail can be found in (Dunne et al., 2007).

At a given loading instant, the total deformation gradient $\boldsymbol{F}$ is decomposed into two components, namely the elastic $\boldsymbol{F^e}$ and plastic $\boldsymbol{F^p}$ deformation gradients as

$$\boldsymbol{F} = \boldsymbol{F^e F^p} \tag{1}$$

The plastic velocity gradient $\boldsymbol{L^p}$ is obtained from summing the slip rates $\dot{\gamma}^{(i)}$ along all active slip systems, given by

$$\boldsymbol{L^p} = \sum_{i=1}^{M} \dot{\gamma}^{(i)} \boldsymbol{s}^{(i)} \otimes \boldsymbol{n}^{(i)} \tag{2}$$

where M is the total number of slip systems ($M = 12$ for an FCC crystal), $\boldsymbol{s}^{(i)}$ and $\boldsymbol{n}^{(i)}$ are the slip and normal vector directions of the i^{th} slip system, respectively. The slip rate $\dot{\gamma}^{(i)}$ along

the i^{th} slip system is given by a slip rule based on thermally activated dislocation escape from obstacles (such as lattice defect, impurities, inclusions, etc), which is given by:

$$\dot{\gamma}^{(i)} = \rho_{ssdm} b^2 v_D \, exp\left(-\frac{\Delta H}{k\theta}\right) sinh\left(\frac{\Delta V}{k\theta}\left|\tau^{(i)} - \tau_c^{(i)}\right|\right) \quad (3)$$

where ρ_{ssdm} is the initial mobile statistically stored dislocation density, b the magnitude of Burgers vector, v_D the frequency of attempted dislocation jumps over obstacles, ΔH the activation energy, θ the temperature, k the Boltzmann constant, ΔV the activation volume, and $\tau^{(i)}$ and $\tau_c^{(i)}$ are the resolved shear stress and critical resolved shear stress on the i^{th} slip system, respectively. The critical resolved shear stress $\tau_c^{(i)}$ evolves with dislocation density, which is correlated with the effective plastic strain, according to a hardening law. The strain rate sensitivity of a slip system is governed by the combination of ΔH and ΔV. The total plastic slip is calculated using:

$$\gamma^{(i)} = \int_0^t \dot{\gamma}^{(i)} \, dt \quad (4)$$

The material properties were determined by calibrating the polycrystal sample response under uniaxial tensile testing (Chen et al., 2017; Guan et al., 2017) and given in

Table 1. In this work with nickel alloy, the activation energy ΔH and volume ΔV were chosen to ensure negligible rate sensitivity at room temperature.

Table 1: CPFE material parameters for nickel-based alloys

Parameter	Value
ρ_{ssdm}	$0.05\mu m^{-2}$
b	$0.351nm$
v_D	$10^{11}Hz$
ΔH	$0.3067ev$
ΔV	$0.237b^3$
k	$1.38 \times 10^{-23} JK^{-1}$
τ_c	$350MPa$

Mechanistic understanding of fatigue crack nucleation is a topic of interest for many researchers, since understanding the key drivers would enable the quantitative correlation between the local deformation and the crack nucleation in engineering alloys. A recent mechanistic criterion (Wan et al., 2014) based on microstructurally local stored energy

density, reflecting dislocation accumulation, has been proposed and captures highly localized crack nucleation in several alloys (Chen et al., 2018, 2017; Wan et al., 2016a, 2014). The stored energy density $\dot{G}$ per loading cycle is given by

$$\dot{G} = \int \frac{\zeta |\boldsymbol{\sigma} : d\boldsymbol{\epsilon^p}|}{\sqrt{\rho_{SSD} + \rho_{GND}}} \tag{5}$$

where ζ is the fraction of the dissipated plastic energy which is stored elastically in dislocation structure formation, $\boldsymbol{\sigma}$ the stress, $\boldsymbol{\epsilon}^p$ the plastic strain, ρ_{SSD} the density of statistically stored dislocations (SSD) evolving with effective accumulated plastic strain and ρ_{GND} is the density of geometry necessary dislocation (GND) obtained from the curl of plastic deformation gradient tensor $\boldsymbol{F^p}$ (Cheng and Ghosh, 2015). Therefore, the evolution of stored energy G accumulates with cycles and is calculated using

$$G = \int \dot{G} dN \tag{6}$$

The argument is then made that the onset of fatigue crack nucleation occurs when the stored energy density achieves a critical value G_c.

2.2 Discrete dislocation plasticity

2.2.1 DD formulation

Planar discrete dislocation plasticity was originally developed by Van der Giessen and Needleman (Giessen and Needleman, 1995), and employs the principle of superposition by Lubarda (Lubarda et al., 1993) to solve individually the problem of interacting dislocations in a homogeneous infinite medium and the problem of the dislocation free body along with its boundary conditions. Based on this approach the displacement ($\boldsymbol{u}$), strain ($\boldsymbol{\varepsilon}$) and stress field ($\boldsymbol{\sigma}$) are partitioned as follows:

$$\boldsymbol{u} = \widetilde{\boldsymbol{u}} + \widehat{\boldsymbol{u}} \qquad \boldsymbol{\varepsilon} = \widetilde{\boldsymbol{\varepsilon}} + \widehat{\boldsymbol{\varepsilon}} \qquad \boldsymbol{\sigma} = \widetilde{\boldsymbol{\sigma}} + \widehat{\boldsymbol{\sigma}} \tag{7}$$

where the (~) fields represent the infinite plane analytical fields of all the edge dislocations in the body and the (^) fields satisfy the following modified boundary value problem as shown schematically in Figure 1:

$$\nabla \cdot \hat{\boldsymbol{\sigma}} = 0$$
$$\hat{\boldsymbol{\sigma}} = \boldsymbol{L}\hat{\boldsymbol{\varepsilon}} \tag{8}$$
$$\hat{\boldsymbol{\varepsilon}} = \frac{1}{2}(\nabla\hat{\boldsymbol{u}} + (\nabla\hat{\boldsymbol{u}})^T)$$

in which $\boldsymbol{L}$ is the fourth order tensor of elastic constants, and

$$\hat{\boldsymbol{\sigma}} \cdot \boldsymbol{n} = \boldsymbol{T} - \tilde{\boldsymbol{\sigma}} \cdot \boldsymbol{n} \ \ on\ \boldsymbol{\Gamma_t} \tag{9}$$
$$\hat{\boldsymbol{u}} = \boldsymbol{u} - \tilde{\boldsymbol{u}} \ \ on\ \boldsymbol{\Gamma_u}$$

where $\boldsymbol{n}$ is the unit normal and $\boldsymbol{\Gamma_t}, \boldsymbol{\Gamma_u}$ the regions on the boundary $\boldsymbol{\Gamma}$ where the tractions and displacements are applied, respectively. Typically, the boundary value problem (^ fields) is solved using the finite element method.

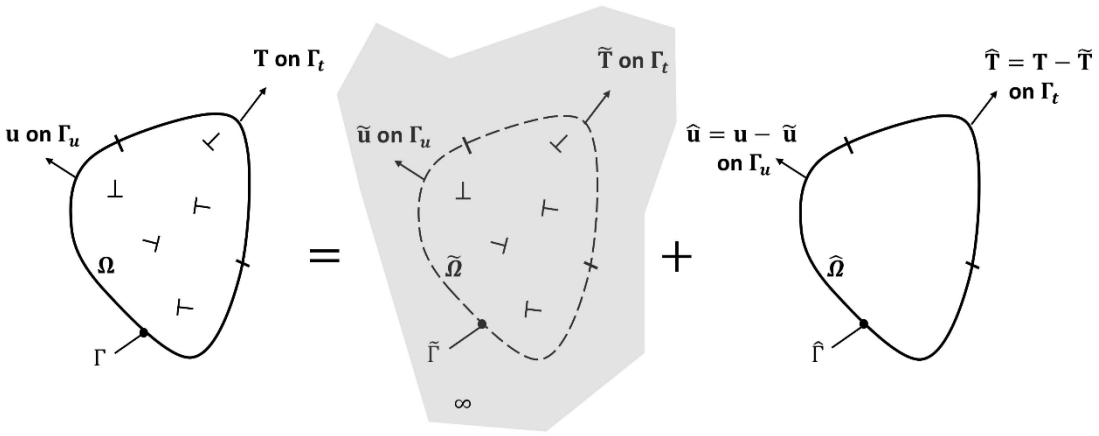


Figure 1: Principle of superposition as applied to a body containing dislocations. The body is decomposed into a problem of interacting dislocations inside an infinite homogeneous medium (~ fields) and a complementary problem for the inhomogeneous body that does not contain dislocations (^ fields).

Dislocations are treated as line singularities with equal Burgers vector magnitude b. Initially the specimen is dislocation free with Frank-Read sources and obstacles randomly distributed on the slip planes. The strength of each source τ_{nuc} is randomly assigned from a Gaussian distribution with average value $\bar{\tau}_{nuc}$ and standard deviation $0.2\bar{\tau}_{nuc}$. Once the resolved shear stress acting on the source exceeds the nucleation stress τ_{nuc} for a period longer than the nucleation time t_{nuc}, a dipole nucleates with a spacing:

$$L_{nuc} = \frac{\mu b}{2\pi(1-\nu)\tau_{nuc}} \tag{10}$$

where μ is the shear modulus and ν Poisson's ratio. Under the influence of external and internal stresses, dislocations may become mobile and glide along their slip planes. The relation between the stress state of the body and the force governing the motion of a dislocation I is

$$f_i^{(I)} = m_i^{(I)} \cdot \left(\hat{\sigma}_{ij} + \sum_{J \neq I} \tilde{\sigma}_{ij}^{(J)} \right) \cdot b_j^{(I)} \tag{11}$$

where $m_i^{(I)}$ the normal to the slip plane containing the dislocation I, $\hat{\sigma}_{ij}$ the image stress at the location of dislocation I, $\tilde{\sigma}_{ij}^{(J)}$ the stress field of dislocation J within the infinite medium and $b_j^{(I)}$ is the Burgers vector. The glide velocity of dislocation I, is linearly related to the Peach-Koehler force with a drag coefficient B_{drag} as

$$v_i^{(I)} = \frac{f_i^{(I)}}{B_{drag}} \tag{12}$$

Two opposite signed dislocations on the same slip plane may annihilate if they fall within a critical distance $L_e = 6b$. Dislocation motion can be hindered by the presence of obstacles and grain boundaries (GBs). Pinned dislocations can overcome the obstacles once their Peach–Koehler force exceeds an obstacle dependent value $\tau_{obs} b$.

The free surfaces of the model are unpassivated and hence dislocations can freely escape, leaving a displacement step of magnitude $b/2$ on the free surface upon their exit. Dislocations remaining inside the crystal could either be geometrically necessary or statistically stored. The former, are dislocations supporting the geometric continuity of the crystal and could be quantified by the dimensionless net Burgers vector within the subdomain divided by its area A_l (Kondori et al., 2017), given by

$$\rho_{GND}(A_l) = \frac{|\sum \boldsymbol{b}|}{b A_l} \tag{13}$$

By definition, the GND density is a length-scale dependent quantity and therefore the subdomain over which it is stored, should be carefully selected with consideration as to how the dislocation density is distributed in the material (Zheng et al., 2019). Statistically stored dislocations arise from random trapping processes and do not have long range geometric effects.

2.2.2 Configurational energy

In this section, a brief description of the theory behind the configurational energy is given. For a more detailed description, the reader is referred to (Zheng et al., 2019).

The free energy Φ stored in a plastically deformed crystal consists of the energy associated with the dislocations W^{dis} and the elastically stored energy W^e,

$$\Phi = W^{dis} + W^e \tag{14}$$

At each stage of loading the elastic stored energy is given by

$$W^e = \frac{1}{2}\int_V \breve{\sigma}\colon \breve{\varepsilon}\, dV \tag{15}$$

where $\breve{\sigma}$ and $\breve{\varepsilon}$ are the stress and strain fields respectively in a dislocation-free body with external tractions applied on the free surfaces of the model (Balint et al., 2008; Deshpande et al., 2005). The dislocations associated energy can be expressed as the sum of the dislocation line energy and the configurational energy given by

$$W^{dis} = E_l + E_{conf} \tag{16}$$

where E_l is the dislocation line energy consisting of the sum of the self and core energies from all the individual dislocations as if they were isolated (Benzerga et al., 2005). The quantity of interest in this work is E_{conf} and represents the interaction energy between dislocations under the current stress state. To derive a functional form for the E_{conf}, the free energy Φ of the system is expressed as (Lubarda et al., 1993)

$$\Phi = \frac{1}{2}\int_V \widehat{\boldsymbol{\sigma}}\colon \hat{\boldsymbol{\varepsilon}} dV + \frac{1}{2}\int_V (\widehat{\boldsymbol{\sigma}}\colon \tilde{\boldsymbol{\varepsilon}} + \tilde{\boldsymbol{\sigma}}\colon \hat{\boldsymbol{\varepsilon}}) dV + \frac{1}{2}\sum_{\substack{j=1 \\ j\neq k}}^{N}\sum_{k=1}^{N}\int_{V^L} \tilde{\boldsymbol{\sigma}}^j\colon \tilde{\boldsymbol{\varepsilon}}^k dV + E_l \tag{17}$$

From equations (14-17), the configurational energy is deduced as:

$$E_{conf} = \frac{1}{2}\int_V \widehat{\boldsymbol{\sigma}}\colon \hat{\boldsymbol{\varepsilon}} dV + \frac{1}{2}\int_V (\widehat{\boldsymbol{\sigma}}\colon \tilde{\boldsymbol{\varepsilon}} + \tilde{\boldsymbol{\sigma}}\colon \hat{\boldsymbol{\varepsilon}}) dV + \frac{1}{2}\sum_{\substack{j=1 \\ j\neq k}}^{N}\sum_{k=1}^{N}\int_V \tilde{\boldsymbol{\sigma}}^{\boldsymbol{j}}\colon \tilde{\boldsymbol{\varepsilon}}^{\boldsymbol{k}} dV - \frac{1}{2}\int_V \breve{\boldsymbol{\sigma}}\colon \breve{\boldsymbol{\varepsilon}} dV \tag{18}$$

The local configurational energy density may be evaluated using

$$U_{conf} = \frac{1}{2}\widehat{\boldsymbol{\sigma}}:\widehat{\boldsymbol{\varepsilon}} + \frac{1}{2}(\widehat{\boldsymbol{\sigma}}:\widetilde{\boldsymbol{\varepsilon}} + \widetilde{\boldsymbol{\sigma}}:\widehat{\boldsymbol{\varepsilon}}) + \frac{1}{2}\sum_{\substack{j=1 \\ j\neq k}}^{N}\sum_{k=1}^{N}\widetilde{\boldsymbol{\sigma}}^{j}:\widetilde{\boldsymbol{\varepsilon}}^{k} - \frac{1}{2}\breve{\boldsymbol{\sigma}}:\breve{\boldsymbol{\varepsilon}} \tag{19}$$

which takes units of $J \cdot m^{-3}$. From U_{conf}, the configurational energy area density G_{conf} can be derived which is argued to be mechanistically important for fatigue crack nucleation and growth (Wilson et al., 2018; Zheng et al., 2019),

$$G_{conf} = \frac{U_{conf}}{\sqrt{\rho_{dis}}} \tag{20}$$

where ρ_{dis} is the total local dislocation density. An appropriate grid size has to be selected for calculating U_{conf} and $1/\rho_{dis}$ which is determined by using convergence studies.

The configurational energy area density is argued to be responsible for driving fatigue crack nucleation when a critical configurational energy has been established. The stored energy density (equation 6) is an attempt at determining (approximately) the same quantity but within a CPFE framework, where discrete dislocations are not explicitly represented. The CPFE calculation provides the plastic dissipation per unit volume, and a small fraction of this plastic work (typically 5%) is argued to be stored in the form of dislocation structures. The stored energy is calculated over an area determined by the dislocation density, calculated here using the dislocation mean free distance. In what follows, it is demonstrated that the CPFE stored energy density provides a good approximation to the discrete dislocation configurational energy density and is therefore a useful quantity in predicting fatigue crack nucleation.

2.2.3 Model calibration

The material properties of the DD model were calibrated against the CPFE model subjected to monotonic load-control uniaxial tension of a single crystal as shown by the schematic in Figure 2(a). Figure 2(b) shows the excellent match between the stress-strain curve obtained from the DD model and that obtained from the CP model (which in turn is obtained from experimental stress-strain data).

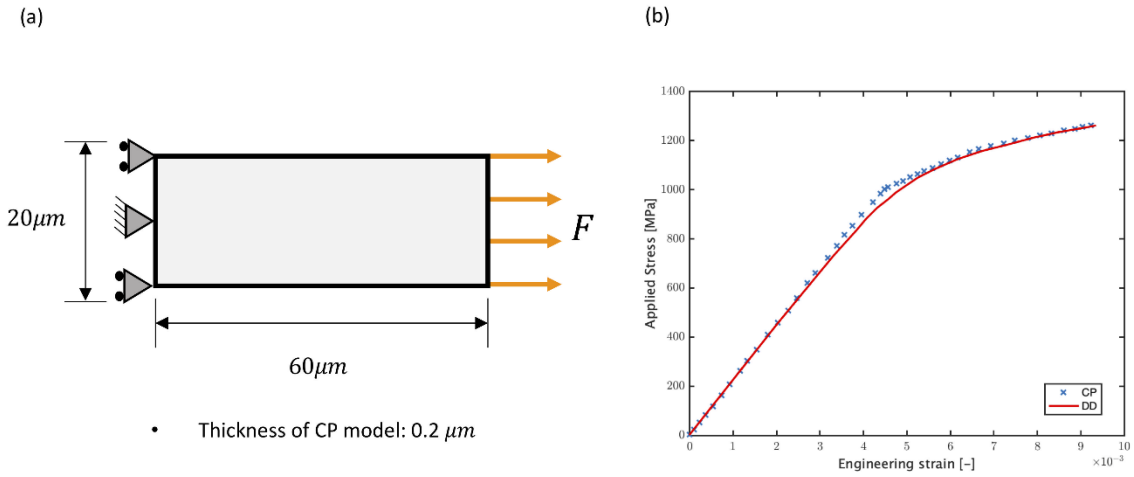


Figure 2:(a) Schematic of the loading and boundary conditions of the model used for the calibration of material parameters of the DD model, (b) Calibration curve showing the fit between the material parameters of the DD model and CPFE model.

Assuming an elastically isotropic single crystal the material properties of the DD model inferred after calibration are given in Table 2. A time step $0.5\ ns$ is required to resolve the dislocation dynamics.

Table 2: Material properties used in the DD model after calibration

Ni superalloy	E (GPa) 200	v $(-)$ 0.31	b (nm) 0.3507	B $(Pa \cdot s)$ 5×10^{-4}
Sources	ρ_s (μm^{-2}) 60	τ_{nuc} (MPa) 600	Source standard deviation (MPa) 120	t_{nuc} (ns) 10
Obstacles	ρ_{obs} (μm^{-2}) 360	τ_{obs} (MPa) 1800	Obstacle standard deviation (MPa) 0	

The total strain (which consists primarily of plastic strain) measured in the experiments (see later) and predicted by CPFE is used as a benchmark against the total slip predicted by the DD model to assess the capability of the DD model in capturing the primary deformation patterns. The total slip Γ is defined as the sum of the resolved strain tensor ε_{ij} over the active slip systems (Balint et al., 2006), expressed as:

$$\Gamma = \sum_{a=1} \left|\gamma^{(a)}\right| = s_i^{(a)} \varepsilon_{ij} m_j^{(a)} \tag{21}$$

where $s_i^{(a)}$ and $m_j^{(a)}$ are the tangent and normal to slip system a respectively. It is useful to note that the DD total slip Γ provides a visualisation of the deformation slip patterns present in the crystal and is not identical to the plastic slip as defined in continuum plasticity and equation 4.

3 Experiment, CP, and DD Modelling of Beam Bending Fatigue in Single Crystal Nickel

In this section, because we aim to establish fully representative DD and CPFE models of the experimental conditions, including the loading and single crystal crystallographic orientation, the independently reported experimental set up is briefly described, followed by the construction of the CPFE and the DD geometric models.

3.1 Experimental set up

The single crystal beams (SX1, SX2) used in the experiments and CPFE (Chen et al., 2017; Guan et al., 2017) have dimensions $\mathrm{L} \times \mathrm{W} \times \mathrm{H} = 12 \times 3 \times 3$ mm and crystal orientation given by the three Euler angles (Bunge notation) $[244° \; 32° \; 141°]$ and $[85° \; 5° \; 263°]$ respectively. Crystallographic information was obtained using electron backscattered diffraction (EBSD) on the (front) free surface, and high-resolution digital image correlation (HR-DIC) measurements of strain were recorded on the (back) free surface. The schematic diagrams in Figure 3 (a,b) illustrate the boundary conditions relating to the experiment and the CPFE model, with an inset illustrating the projection of activated slip systems onto the free surface. The beams were cyclically loaded at a loading ratio R=0.1 with the peak loading increasing after the first 800 cycles to increase the rate of slip accumulation (Figure 3 (c)). Relevant crystallographic information is given in Appendix A. Comprehensive reports on the cyclic three-point experiment methodology, DIC strain measurement and EBSD orientation mapping on a range of nickel alloys can be found in (Guan et al., 2017; Jiang et al., 2015).

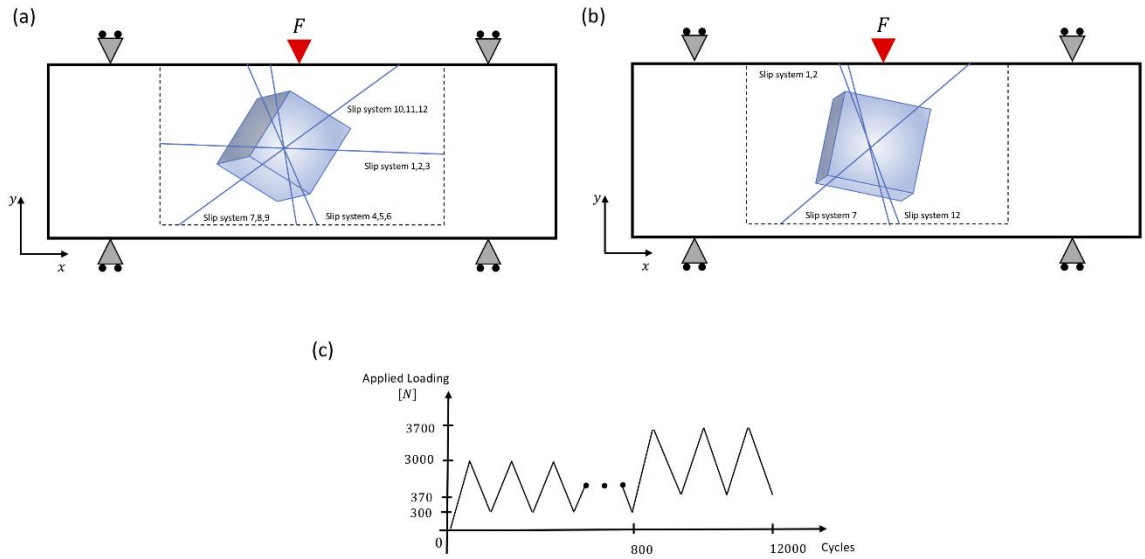


Figure 3: Applied boundary conditions and inset illustrating the crystallographic orientation of crystal with projection of the slip systems onto the free surface for single crystal (a) SX1 and (b) SX2 and (c) loading history of single crystals.

3.2 CPFE model setup

The boundary conditions and loading history applied on the single crystal specimens in the CPFE modelling replicate those in the bending tests that are shown in Figure 3. The CPFE model assigns five small elastic regions located around the supporting loading sites to avoid artificial stress concentrations, and it is discretised using 2400 quadratic finite elements. Mesh sensitivity studies were conducted, and it was established that further refinement of the mesh did not affect the numerical results.

3.3 DD model setup

Prior to developing the DD model, there are some fundamental differences that need to be considered in order to create an accurate and reliable comparison between experiment, CPFE and DD. Firstly, DD is a 2-D plane strain modelling technique and therefore cannot capture the out-of-plane strains, which are indeed present in the experiments. To resolve this issue, the slip systems in the DD model are taken to be the projection of the activated slip systems onto the free surface of the beams as shown in Figure 3(a,b). For SX1, the slip direction projections of systems 3, 8 and 10 (nomenclature provided in Appendix A) were explicitly represented in the DD model. The family of slip systems 4,5 and 6 was omitted in the DD model, as it showed no significant slip activation compared to the other families of slip systems (Guan et al., 2017). An additional consideration is the difference in the length scales

associated with the CP and DD modelling. The former (CP) model replicates the experimental sample dimensions. However, this is problematic for the DD analysis simply because of excessive computer run times. Hence to facilitate a one-to-one comparison, a geometrically similar model was devised within the DD framework that replicates the boundary conditions applied in the experiments and CPFE but which is scaled to a much smaller size, thus reducing CPU times, but not so small as to inappropriately lead to significant increases in GND density through the size effect. Local to the supports and loading point in the DD model (and the CPFE), elastic zones are introduced to avoid stress singularities. Due to the computationally expensive nature of DD simulations, it is regrettably not feasible to simulate the hundreds, or indeed thousands of cycles performed in the experiments. Hence, only a representative number of cycles are simulated in the DD modelling.

Figure 4 illustrates the geometry and boundary conditions of the DD model along with crystallographic information for the SX1 crystal.

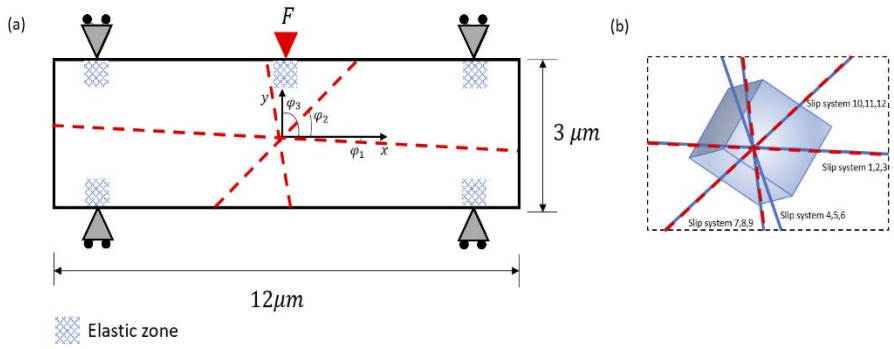


Figure 4: (a) Geometry and boundary conditions of the DD model for the SX1 crystal (b) projection of the slip systems onto the free surface of the single crystal.

The slip plane angles are $\varphi_1 = 0.7°, \varphi_2 = 42°, \varphi_3 = 106°$. The single crystal is discretised with 120×30 quadratic finite elements to solve the boundary condition problem. A similar methodology is employed for the second single crystal (SX2) test.

4 Results and discussion

Two key experimental observations are to be used to assess the role of configurational energy density in driving fatigue crack nucleation. The first is the crystallographic slip activations observed in the experiments (Guan et al., 2017) and the second, the sites of fatigue crack nucleation in the experiments by (Chen et al., 2017), both respectively addressing single

crystal nickel fatigue. The DD model predictions of slip and of configurational energy density are compared directly with experimental observations of fatigue crack nucleation, and with the results of CPFE modelling.

Figure 5 shows a qualitative comparison between experiment and the computational models for the first single crystal, SX1. From the experiment, a clear demarcation between slipped and non-slipped regions was observed. The overall slip field is asymmetric due to the misorientation between the crystal's principal axes and the loading axis. A strong localisation, in the form of discrete and well separated slip bands is revealed in the central bottom region of the beam, which is indicative of the predominantly single slip taking place during the early stages of deformation. With the development of accumulative plastic strain, secondary slip is activated, and gives rise to a more homogeneous distribution of the developed plastic strains, as can be seen in the inset of Figure 5(b). The primary slipped region develops from the activation of one or more slip systems that belong to the 10,11,12 group of slip systems. An interesting observation is the formation of a secondary slipped region near the beam's neutral axis by one of the slip systems of the 1,2 or 3 group, indicated by the red encircled area in Figure 5(b). Details of the experimental observations can be seen in Figure 5(b).

Nonetheless, the deformation pattern predicted by the DD model after 5 cycles exhibits similar behaviour with the experiment and CPFE model (Guan et al., 2017) as can be seen by Figure 5(c). In particular, the slip bands predicted by the DD model in the lower central region of the beam and along its neutral axis, seem to correlate well with those observed in experiment and CPFE. The slip asymmetry and heterogeneity are also well captured by the DD model.

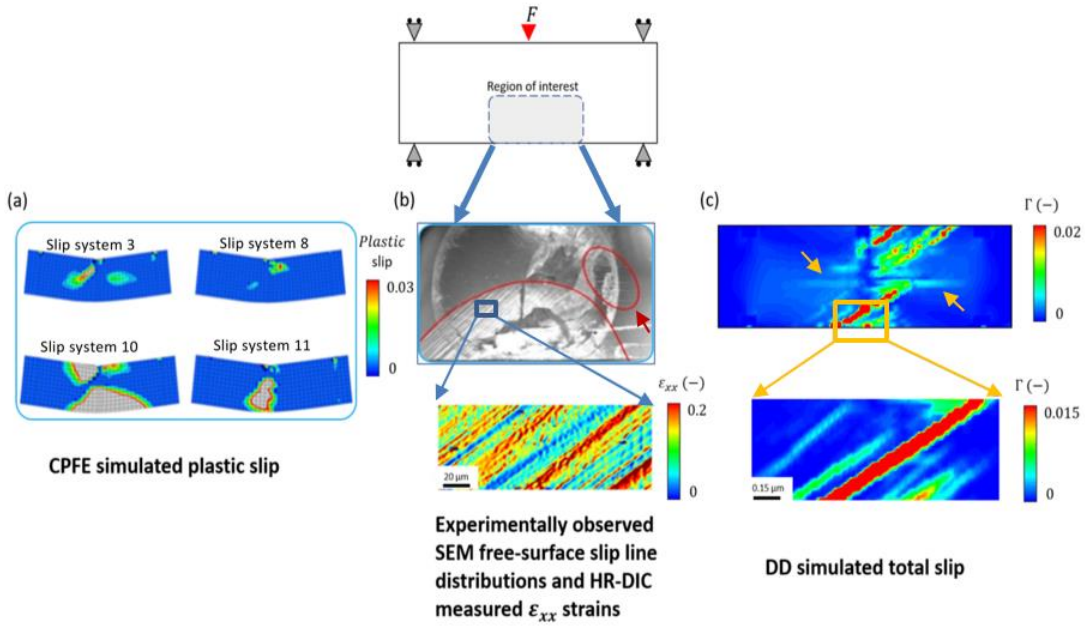


Figure 5: (a) Spatial distributions of the CPFE predicted slip for each activated slip system in SX1, (b) experimentally observed slip line distribution using SEM and spatial distribution of the ε_{xx} strains measured using HR-DIC (Guan et al., 2017), (c) spatial distribution of the total slip predicted by the DD model after 5 cycles.

4.1 Predicting crack nucleation site using energy criterion

The DD and CPFE models predict the distributions of dislocation configurational and stored energy densities respectively. The results for the first single crystal (SX1) are shown in Figure 6(a-f) which illustrates qualitative comparisons between the stored and configurational energy densities at the end of 1st, 5th and 10th cycles of loading. Both quantities from the two models respectively predict that the highest energy densities develop at the bottom centre of the beam free surface, co-located with the predominant slip region, and highest bending stresses in that region. Plasticity is largely confined within the lower central region of the beam while much of the remainder of the beam, including some areas along the neutral axis, remain mostly elastic. On a qualitative level, the contour plots of the DD configurational energy density reveal a more discrete map of the energy hot spots compared to the CP stored energy maps, due to the inherent discreteness of dislocation structures.

By using three-point bending, the region of crack nucleation is confined within the general region of the beam between the supports, i.e. at the lower central region of the beam.

However, because the single crystal major axes do not align with the loading direction, the resulting deformation and stress states are neither symmetric nor bottom centre of the beam.

To assess quantitatively whether the configurational energy density captures the location of the experimentally observed crack nucleation site (and hence the predicted CP peak stored energy), the energy density distributions along the bottom surface of the beam through the paths x-x' in Figure 6(a,d) are extracted and compared in Figure 6 (g-i). It is noted that the energy distribution in DD is strongly affected by the position of the chosen path, e.g. if the chosen path passes through a group of dislocations, the energy at that location becomes much higher than the average energy. For this reason, an average of the energy density distribution along 6 paths which are all parallel to and within $0.5\mu m$ from the bottom surface is assessed to compare with CPFE calculations. The path x-x' in each model is normalised by its respective crystal width. Clearly, and as anticipated, the DD energy is more discrete in nature than the corresponding CP stored energy. The DD energy shows a higher rate of increase in the magnitude of configurational energy with cycles, but both quantities nonetheless are of similar magnitude and in addition, coincide with respect to the location of highest energy along the beam. The contour plots in Figure 6(a-f) focus only on the bottom half of the beams, which is the region of interest for fatigue crack nucleation.

At the end of the first cycle, in Figure 6 (g), the configurational energy density exhibits a clear peak which coincides with the experimentally observed crack nucleation site (indicated by the vertical red line), and with the location of the peak CPFE stored energy density. As the cyclic loading progresses (5^{th} and 10^{th} cycles), the peak configurational energy increases and remains very close to the location of the crack nucleation site while the energy gap between the peak configurational energy and stored energy narrows.

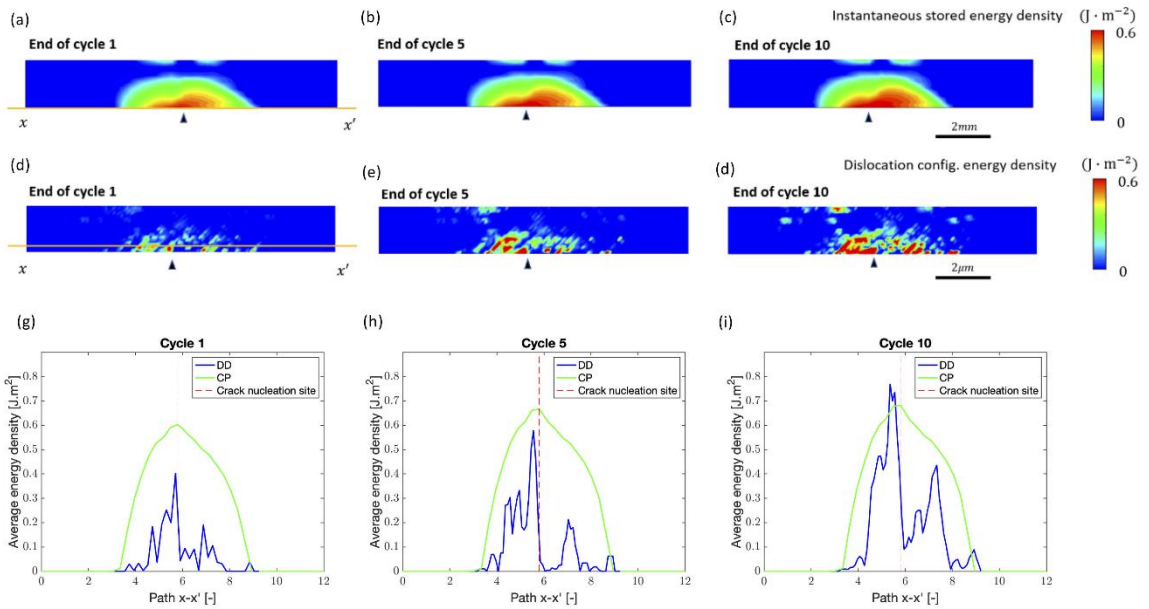


Figure 6: (a-c) Contour maps of stored energy density (CPFE) and (d-f) configurational energy density (DD) of the bottom half of the beams. The black triangles indicate the experimentally observed location of crack nucleation in single crystal SX1. (g-i) show quantitative comparisons between the two quantities along the paths x-x'. Note: the path x-x' in both models is normalised by the width of the respective crystals.

Figure 7 illustrates a more quantitative comparison of the evolution of stored and configurational energy densities, over ten cycles for the region of interest located around the experimentally observed crack nucleation site ($\approx \frac{x}{W} = 0.48$). It is clear that with progressing cycling loading, the difference between the magnitude of the configurational energy density and the stored energy decreases which is in keeping with the observations in (Zheng et al., 2019). The stored energy density appears to evolve more slowly with cycles, while the configurational energy increases sharply between cycles 1 to 6 and achieves a steadier evolution rate from cycle 6.

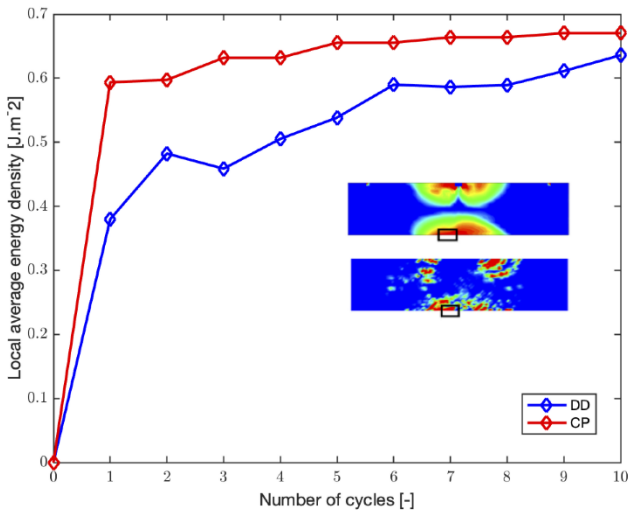


Figure 7: Evolution of stored and configurational energy densities over 10 cycles. The region of interest selected, is identical in both beams.

Following the above methodology, another DD model was developed to simulate the second nickel single crystal (SX2) that was subjected to fatigue loading leading to crack nucleation in a previous study (Chen et al., 2017). The qualitative and quantitative comparisons between CPFE, DD and the experimentally observed crack nucleation site for SX2 are shown in Figure 8 (a-i), and as in the previous single crystal experiment, the DD configurational energy and CP stored energy densities both capture the same locations of energy peaks in the crystal which again coincide with the experimentally observed crack nucleation site.

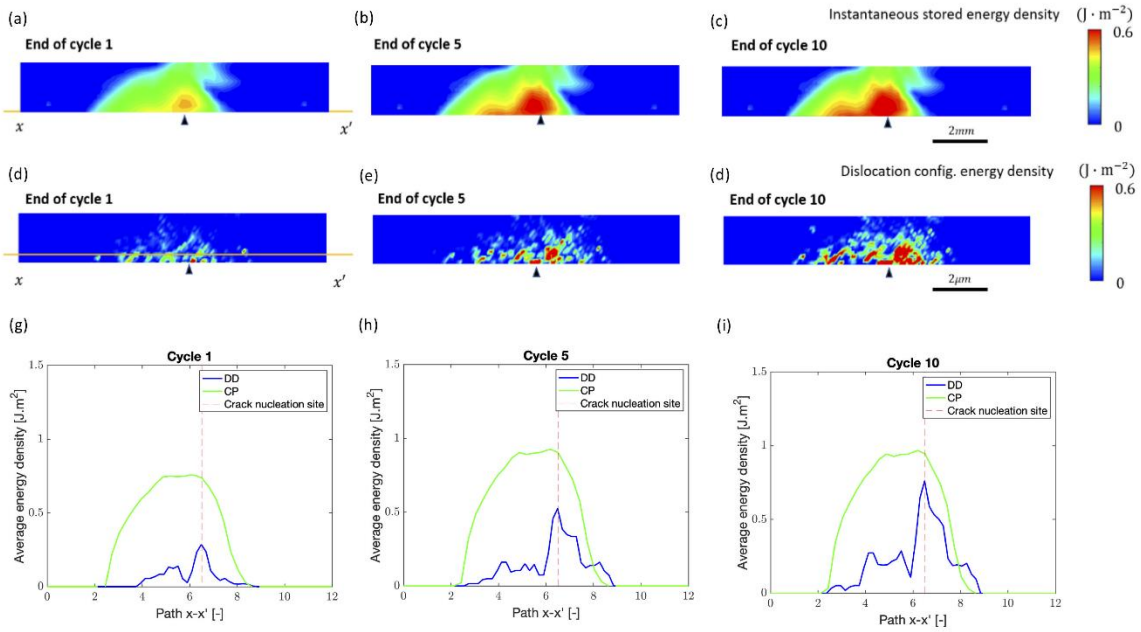


Figure 8: (a-c) Contour maps of stored energy density (CPFE) and (d-f) configurational energy density (DD) of the bottom half of the beams. The black triangles indicate the experimentally

observed location of crack nucleation in single crystal SX2. (g-i) show quantitative comparisons between the two quantities along the paths x-x'. Note: the path x-x' in both models is normalised by the width of the respective crystals.

4.2 GND density and lattice rotation near crack nucleation sites

In the previous experimentally validated CPFE modelling studies on nickel superalloys (Chen et al., 2018, 2017; Wan et al., 2016a), it is argued that key microstructurally sensitive quantities including GND and SSD densities are potentially important precursors of fatigue crack nucleation. However, it was demonstrated that no one quantity (slip, stress, SSD nor GND density) unambiguously predicted the experimentally observed fatigue crack nucleation sites (as opposed to the stored energy density which did). Indeed, as can be seen in Figure 9 (a-c) which relates to the first single crystal (SX1), the contour plots of the GND density from the CPFE model do not reveal any clear relationship between locations of high GND density and the observed experimental crack nucleation site (black triangles). Using equation (13) and a Burgers circuit area of $\mathrm{A_l} = 0.1 \times 0.1\ \mu m^2$, the GND density predicted by the DD model is shown in Figure 9 (d-f), and indicates a more widespread distribution with higher magnitude throughout the single crystal, with the majority of high densities locating at the central bottom region of the beam.

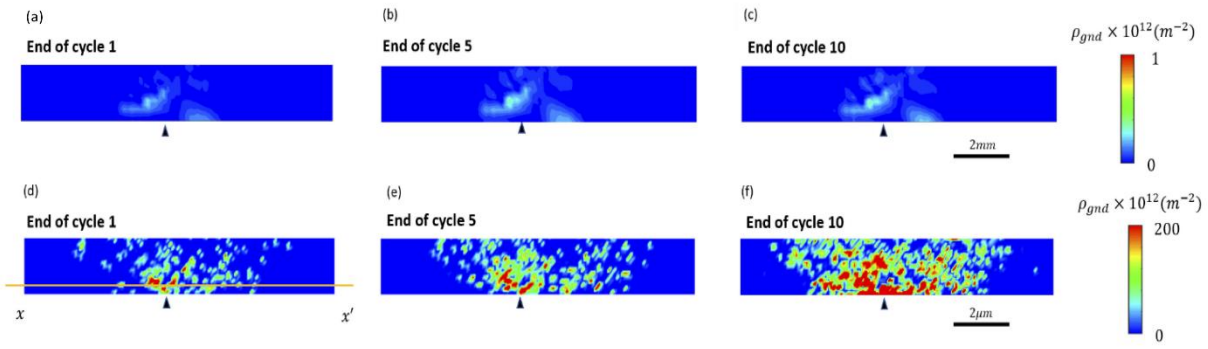


Figure 9: (a-c) GND density predicted by the CPFE model and (d-f) GND density predicted by the DD model for the first Ni single crystal (SX1).

GND density is a length-scale dependent quantity and as a consequence of the DD model beam being considerably smaller than that utilised for the CPFE calculations (for the reasons discussed above), the GND densities predicted by the DD model are considerably higher, due to the difference in length scale. Nonetheless Figure 10, which shows the distributions of GND and SSD densities along the x-x' path (averaged as previously) of the two single crystal beams (SX1,SX2), does suggest that the GND density plays a role in the identification of fatigue

crack nucleation at the micron length-scale. The peak GND density predicted by DD in both single crystals is close to the location of the crack nucleation site, suggesting that GND density could potentially be an important mechanistic driver of fatigue failure at smaller length scales. Interestingly in the SX1 model, the SSD density seems also to correlate with the crack location but this is not observed in the case of SX2.

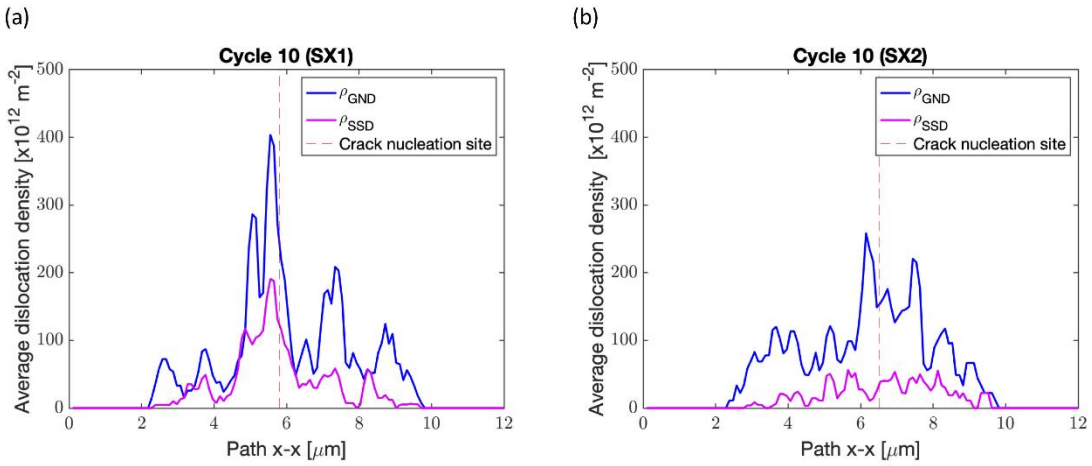


Figure 10: Average GND and SSD density profile along the x-x' path at the end of cycle 10 for (a) SX1 and (b) SX2 single crystal. The dashed line illustrates the location of the experimentally observed primary crack nucleation site.

The lattice rotation, effective strain and principal stresses in the xx direction are also evaluated along the x-x' path for single crystals SX1 and SX2 (relevant equations can be found in Appendix B). The lattice rotation distribution in the SX1 single crystal shown in Figure 11 (a), exhibits a positive peak correlating with the crack nucleation site but this is not the case for the SX2 single crystal shown in Figure 11 (d) which appears to form a discontinuity near the crack site. The effective strain distribution in the SX1 crystal in Figure 11 (b) indicates a sharp drop in strain at the location of the crack nucleation site. However, this is not repeated for the SX2 crystal in Figure 11 (e), where similarly, no peak uniquely identifies the crack site. The bending stress component σ_{xx} shown in Figure 11 (c,f) does not exhibit any peak that unambiguously correlates with the location of the observed crack sites in the experiments. All the observations lead to the conclusion that the local lattice rotation, effective strain, stress, SSD density and GND density may be important precursors of fatigue crack nucleation but do not independently identify where cracks nucleate. However, in this study, the GND density is clearly important and as has been noted in previous work, the GND density appears to be a much stronger contributor to both configurational energy and stored energy densities,

and it is notable that this of course relates to lattice curvature. The nucleation of a crack potentially facilitates the release of the curvature and hence of the stored energy which may be the driver of the new free surface energy.

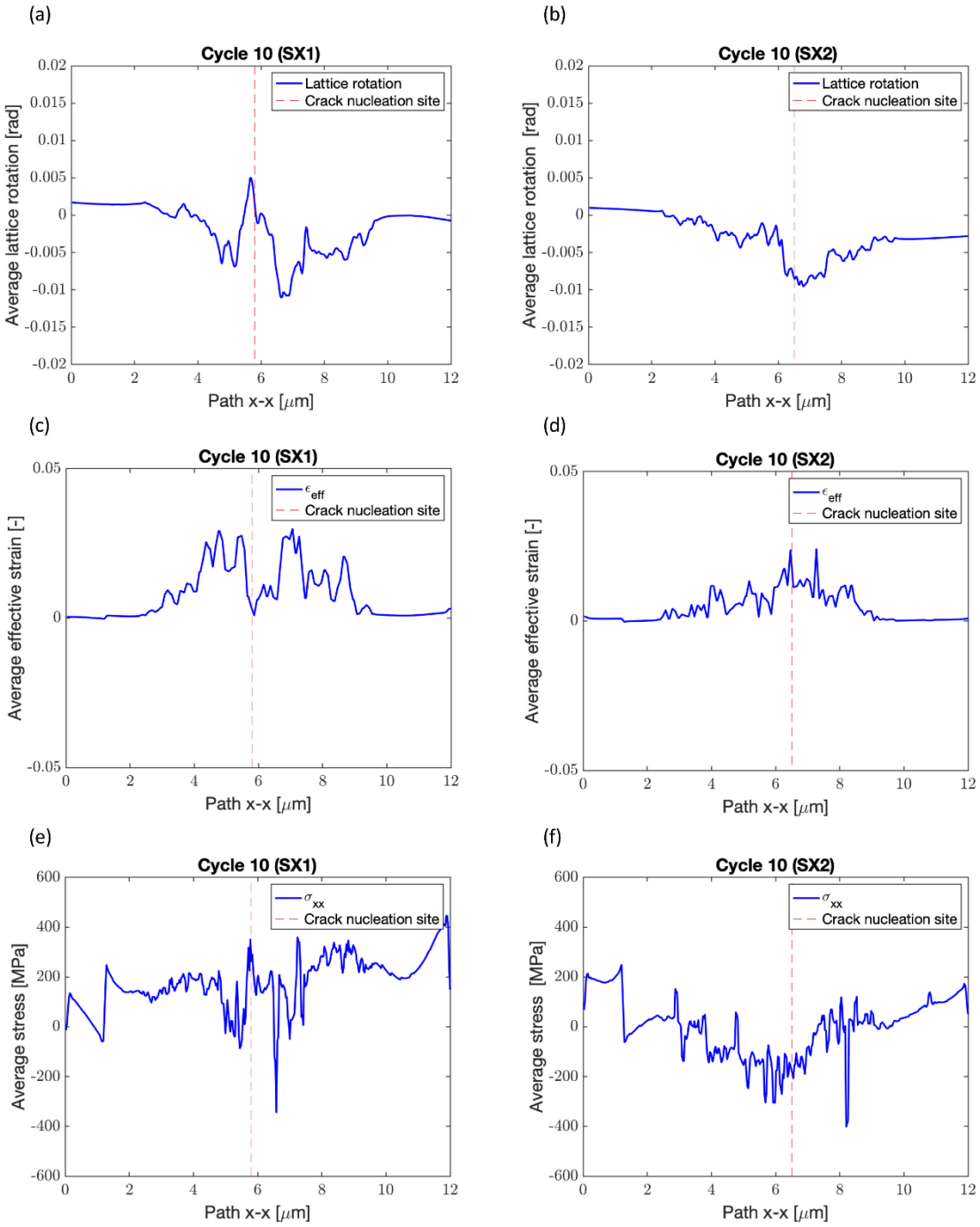


Figure 11: Average distribution of lattice rotation, effective strain and σ_{xx} along the path x-x' for single crystals SX1 (a,c,e) and SX2 (b,d,f), respectively. The primary crack nucleation site observed in the experiments is indicated by the vertical dashed red line.

5 Conclusion

Dislocation configurational energy density (from DD) and stored energy density (from CPFE) have been determined for experimental single crystal beam fatigue and assessed as drivers of fatigue crack nucleation. The key outcomes are as follows:

1. The experimentally observed slip activation in single crystal bend testing has been successfully captured by plane strain DD modelling, replicating the discrete nature of the SEM observations, and the continuum distributions from CPFE modelling. Importantly, the DD configurational energy density and the CPFE stored energy density both correctly identify the location of fatigue crack nucleation in two independent experiments.
2. The configurational energy density distributions were shown to be qualitatively and reasonably quantitatively close to the stored energy densities, and particularly in peak magnitude and peak location. These results reinforce the belief that the former is a key mechanistic factor in fatigue crack nucleation and growth.
3. The role of GND density as a precursor to fatigue crack nucleation was assessed and at appropriate length scales (i.e. micron scale), the GND density plays a significant role in the identification of crack nucleation sites. It is postulated that the release of the energy stored by lattice curvature (i.e. GND structure) is a driver for the generation of new free surfaces (i.e. crack nucleation).
4. Other microstructural quantities such as lattice rotation, principal stress, effective strain and SSD density do not in their own right act as good indicators of crack nucleation sites.

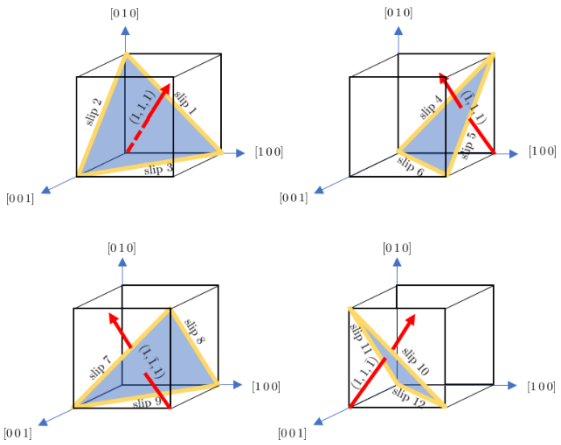
Acknowledgments

N.Prastiti was supported through a studentship in the Centre for Doctoral Training on Theory and Simulation of Materials at Imperial College London funded by the EPSRC (EP/L015579/1).

Appendix A

Crystallographic information of the slip systems in FCC crystals:

(a)



(b)

Slip system	Slip plane	Slip Direction
1	(1,1,1)	[1 -1 0]
2		[0 1 -1]
3		[1 0 -1]
4	(-1,1,1)	[1 1 0]
5		[0 1 -1]
6		[1 0 1]
7	(1,-1,1)	[1 1 0]
8		[0 1 1]
9		[1 0 -1]
10	(1,1,-1)	[1 -1 0]
11		[0 1 1]
12		[1 0 1]

Figure 12: (a) and (b) Illustration of FCC slip system nomenclature used and direction of slip and slip plane normal with respect to an orthogonal (x,y,z) reference system.

Appendix B

In the calculations, the lattice rotation θ is calculated using:

$$\theta = \frac{1}{2}\left(\hat{u}_{2,1} + \tilde{u}_{2,1} - \hat{u}_{1,2} - \tilde{u}_{1,2}\right) \tag{B.1}$$

where subscripts indicate differentiation of the displacement field components with respect to the relevant direction.

The total effective strain in DD is defined as:

$$\varepsilon_{eff} = \sqrt{\frac{2}{3}\left(\varepsilon_{xx}^2 + \varepsilon_{yy}^2 + 2\varepsilon_{xy}^2\right)} \tag{B.2}$$

References

Amodeo, R.J., Ghoniem, N.M., 1990. Dislocation dynamics. II. Applications to the formation of persistent slip bands, planar arrays, and dislocation cells. Phys. Rev. B 41, 6968–6976. https://doi.org/10.1103/PhysRevB.41.6968

Balint, D.S., Deshpande, V.S., Needleman, A., Giessen, E. Van der, 2006. Size effects in uniaxial deformation of single and polycrystals: a discrete dislocation plasticity analysis. Model. Simul. Mater. Sci. Eng. 14, 409–422. https://doi.org/10.1088/0965-0393/14/3/005

Balint, D.S., Deshpande, V.S., Needleman, A., Van der Giessen, E., 2008. Discrete dislocation plasticity analysis of the grain size dependence of the flow strength of polycrystals. Int. J. Plast. 24, 2149–2172. https://doi.org/10.1016/J.IJPLAS.2007.08.005

Benzerga, A.A., Brechet, Y., Needleman, A., Van der Giessen, E., 2005. The stored energy of cold work: predictions from discrete dislocation plasticity. Acta Mater. 53, 4765–4779.

Brinckmann, S., Giessen, E., 2007. A fatigue crack initiation model incorporating discrete dislocation plasticity and surface roughness. Int. J. Fract. 148, 155–167. https://doi.org/10.1007/s10704-008-9190-x

Carpinteri, A., 1994. Handbook of fatigue crack propagation in metallic structures. Volume 2. Elsevier.

Chan, K.S., 2010. Roles of microstructure in fatigue crack initiation. Int. J. Fatigue 32, 1428–1447. https://doi.org/10.1016/J.IJFATIGUE.2009.10.005

Chen, B., Jiang, J., Dunne, F.P.E., 2018. Is stored energy density the primary meso-scale mechanistic driver for fatigue crack nucleation? Int. J. Plast. 101, 213–229. https://doi.org/10.1016/J.IJPLAS.2017.11.005

Chen, B., Jiang, J., Dunne, F.P.E., 2017. Microstructurally-sensitive fatigue crack nucleation in Ni-based single and oligo crystals. J. Mech. Phys. Solids 106, 15–33. https://doi.org/10.1016/j.jmps.2017.05.012

Cheng, J., Ghosh, S., 2015. A crystal plasticity FE model for deformation with twin nucleation in magnesium alloys. Int. J. Plast. 67, 148–170. https://doi.org/10.1016/J.IJPLAS.2014.10.005

Déprés, C., Prasad Reddy, G.V., Robertson, C., Fivel, M., 2014. An extensive 3D dislocation dynamics investigation of stage-I fatigue crack propagation. Philos. Mag. 94, 4115–4137. https://doi.org/10.1080/14786435.2014.978830

Déprés, C., Robertson, C.F., Fivel, M.C., 2004. Crack initiation in fatigue: experiments and three-dimensional dislocation simulations. Mater. Sci. Eng. A 387–389, 288–291. https://doi.org/10.1016/j.msea.2003.12.084

Deshpande, V.S., Needleman, A., Van der Giessen, E., 2005. Discrete dislocation plasticity analysis of single slip tension. Mater. Sci. Eng. A 400–401, 154–157. https://doi.org/10.1016/j.msea.2005.02.087

Deshpande, V.S., Needleman, A., Van der Giessen, E., 2004. Discrete Dislocation Predictions of Single Crystal Fatigue Crack Growth. Springer, Dordrecht, pp. 79–86. https://doi.org/10.1007/978-1-4020-2111-4_8

Dunne, F.P.E., Rugg, D., Walker, A., 2007. Lengthscale-dependent, elastically anisotropic, physically-based hcp crystal plasticity: Application to cold-dwell fatigue in Ti alloys. Int. J. Plast. 23, 1061–1083. https://doi.org/10.1016/j.ijplas.2006.10.013

Giessen, E. Van Der, Needleman, A., 1995. Discrete dislocation plasticity: a simple planar model. Model. Simul. Mater. Sci. Eng. 3, 689–735. https://doi.org/10.1088/0965-0393/3/5/008

Grilli, N., Janssens, K.G.F., Nellessen, J., Sandlöbes, S., Raabe, D., 2018. Multiple slip dislocation patterning in a dislocation-based crystal plasticity finite element method. Int. J. Plast. 100, 104–121. https://doi.org/10.1016/J.IJPLAS.2017.09.015

Guan, Y., Chen, B., Zou, J., Britton, T. Ben, Jiang, J., Dunne, F.P.E., 2017. Crystal plasticity modelling and HR-DIC measurement of slip activation and strain localization in single and oligo-crystal Ni alloys under fatigue. Int. J. Plast. 88, 70–88. https://doi.org/10.1016/J.IJPLAS.2016.10.001

Harvey, S.E., Marsh, P.G., Gerberich, W.W., 1994. Atomic force microscopy and modeling of fatigue crack initiation in metals. Acta Metall. Mater. 42, 3493–3502. https://doi.org/10.1016/0956-7151(94)90481-2

Heinrich, C., Sundararaghavan, V., 2017. A method to predict fatigue crack initiation in metals using dislocation dynamics. Corros. Rev. 35, 325–341. https://doi.org/10.1515/corrrev-2017-0045

Hussein, A.M., El-Awady, J.A., 2016. Quantifying dislocation microstructure evolution and cyclic hardening in fatigued face-centered cubic single crystals. J. Mech. Phys. Solids 91, 126–144. https://doi.org/10.1016/J.JMPS.2016.03.012

Irastorza-Landa, A., Van Swygenhoven, H., Van Petegem, S., Grilli, N., Bollhalder, A., Brandstetter, S., Grolimund, D., 2016. Following dislocation patterning during fatigue. Acta Mater. 112, 184–193. https://doi.org/10.1016/J.ACTAMAT.2016.04.011

Jiang, J., Yang, J., Zhang, T., Dunne, F.P.E.E., Britton, T. Ben, 2015. On the mechanistic basis of fatigue crack nucleation in Ni superalloy containing inclusions using high resolution electron backscatter diffraction. Acta Mater. 97, 367–379. https://doi.org/10.1016/J.ACTAMAT.2015.06.035

Kondori, B., Needleman, A., Amine Benzerga, A., 2017. Discrete dislocation simulations of compression of tapered micropillars. J. Mech. Phys. Solids 101, 223–234. https://doi.org/10.1016/j.jmps.2017.01.015

Krupp, U., 2007. Fatigue crack propagation in metals and alloys. Mater. Today 10, 53. https://doi.org/10.1016/s1369-7021(07)70180-3

Laird, C., Feltner, C., 1968. Factors influencing dislocation structures in fatigued metals. Trans. Metall. Soc. AIME 242.

Lubarda, V.A.A., Blume, J.A.A., Needleman, A., 1993. An analysis of equilibrium dislocation distributions. Acta Metall. Mater. 41, 625–642. https://doi.org/10.1016/0956-7151(93)90092-7

McDowell, D.L., Dunne, F.P.E., 2010. Microstructure-sensitive computational modeling of

fatigue crack formation. Int. J. Fatigue 32, 1521–1542.

Mughrabi, H., 1983. Dislocation wall and cell structures and long-range internal stresses in deformed metal crystals. Acta Metall. 31, 1367–1379. https://doi.org/10.1016/0001-6160(83)90007-X

Paris, P., Erdogan, F., 1963. A Critical Analysis of Crack Propagation Laws. J. Basic Eng. 85, 528. https://doi.org/10.1115/1.3656900

Polák, J., Kruml, T., Degallaix, S., 1993. Dislocation substructure in fatigued duplex stainless steel. Scr. Metall. Mater. 29, 1553–1558. https://doi.org/10.1016/0956-716X(93)90276-X

Sangid, M.D., 2013. The physics of fatigue crack initiation. Int. J. Fatigue 57, 58–72. https://doi.org/10.1016/J.IJFATIGUE.2012.10.009

Suresh, S., 1998. Fatigue of materials, 2nd ed, Choice Reviews Online. Cambridge University Press. https://doi.org/10.5860/choice.29-4547

Tanaka, K., Mura, T., 1981. A dislocation model for fatigue crack initiation. J. Appl. Mech. ASME) 48.1, 97–103.

Tomkins, B., 1968. Fatigue crack propagation—an analysis. Philos. Mag. 18, 1041–1066. https://doi.org/10.1080/14786436808227524

Wan, V.V.C., Jiang, J., MacLachlan, D.W., Dunne, F.P.E., 2016a. Microstructure-sensitive fatigue crack nucleation in a polycrystalline Ni superalloy. Int. J. Fatigue 90, 181–190. https://doi.org/10.1016/J.IJFATIGUE.2016.04.013

Wan, V.V.C., MacLachlan, D.W., Dunne, F.P.E., 2016b. Integrated experiment and modelling of microstructurally-sensitive crack growth. Int. J. Fatigue 91, 110–123. https://doi.org/10.1016/J.IJFATIGUE.2016.05.027

Wan, V.V.C., MacLachlan, D.W., Dunne, F.P.E., 2014. A stored energy criterion for fatigue crack nucleation in polycrystals. Int. J. Fatigue 68, 90–102.

Wilson, D., Zheng, Z., Dunne, F.P.E., 2018. A microstructure-sensitive driving force for crack growth. J. Mech. Phys. Solids 121, 147–174. https://doi.org/10.1016/J.JMPS.2018.07.005

Zheng, Z., Prastiti, N.G., Balint, D.S., Dunne, F.P.E., 2019. The dislocation configurational energy density in discrete dislocation plasticity. J. Mech. Phys. Solids 129, 39–60. https://doi.org/10.1016/j.jmps.2019.04.015